Published in final edited form as:
Cell. 2012 November 21; 151(5): 1029–1041. doi:10.1016/j.cell.2012.10.038.

Three-Dimensional Architecture of the Rod Sensory Cilium and its Disruption in Retinal Neurodegeneration

Jared C. Gilliam[1,5], **Juan T. Chang**[1,2,5], **Ivette M. Sandoval**[1], **Youwen Zhang**[4], **Tiansen Li**[3], **Steven J. Pittler**[4], **Wah Chiu**[1,2], and **Theodore G. Wensel**[1]

[1]Verna and Marrs McLean Department of Biochemistry and Molecular Biology, Baylor College of Medicine, Houston, TX 77030, USA

[2]National Center for Macromolecular Imaging, Baylor College of Medicine, Houston, TX 77030, USA

[3]Neurobiology, Neurodegeneration and Repair Laboratory, National Eye Institute, Bethesda, MD 20892, USA

[4]Dept. of Vision Science, University of Alabama, Birmingham, Birmingham, AL 35924, USA

Summary

Defects in primary cilia lead to devastating disease due to their roles in sensation and developmental signaling, but much is unknown about ciliary structure and mechanisms of their formation and maintenance. We used cryo-electron tomography to obtain three-dimensional maps of the connecting cilium and adjacent cellular structures of a modified primary cilium, the rod outer segment, from wildtype and genetically defective mice. The results reveal the molecular architecture of the cilium and provide insights into protein functions. They suggest that the ciliary rootlet is involved in cellular transport and stabilizes the axoneme. A defect in the BBSome membrane coat caused vesicle targeting near the base of the cilium. Loss of the proteins encoded by the *Cngb1* gene disrupted links between the disk and plasma membranes. The structures of the outer segment membranes support a model for disk morphogenesis in which basal disks are enveloped by the plasma membrane.

Introduction

The first steps of dim-light vision in the vertebrate retina occur in the rod outer segment (OS), a modified primary cilium. The rodent rod OS contains on the order of 1000 lamellar disk membranes containing rhodopsin and phototransduction proteins. Disks are continually shed at the distal OS and phagocytosed by pigmented epithelial cells (LaVail, 1976; Young, 1967). They are replaced by new disks at the base of the OS, requiring large amounts of protein and membrane to be synthesized in the inner segment (IS) of the cell and trafficked to the OS through a ciliary transition zone known as the connecting cilium (CC). The base of the CC is anchored to the cell by a striated rootlet which extends 50 μm or more to the synaptic terminus (Spira and Milman, 1979). A poorly-defined matrix of protein, called the pericentriolar material, surrounds the basal bodies in this region (Moser et al., 2009). The

twensel@bcm.edu.

[5]These authors contributed equally to this work.

pericentriolar material and rootlet are commonly associated with cilia, and both have been proposed as sites of protein targeting and transport (Kim et al., 2004; Yang and Li, 2005), but physical supportive evidence is lacking.

Movement of membrane proteins through the CC is thought to be mediated at least partly by a transport mechanism known as intraflagellar transport (IFT) (Kozminski et al., 1993; Pazour et al., 2002). Many membrane proteins are known to be enriched in photoreceptor (Liu et al., 2007) and other sensory cilia (Gherman et al., 2006; Mayer et al., 2009; Ostrowski et al., 2002), but few authentic IFT cargo proteins have been verified (Nachury et al., 2010). Many soluble proteins are also enriched in the OS. While passive diffusion is a viable method for soluble protein to move through the CC (Calvert et al., 2010; Nair et al., 2005), there may be unknown cytoskeleton-associated mechanisms for directional targeting of soluble proteins through the CC.

The mechanisms by which lipids and membrane proteins synthesized in the IS are transported to the disks of the OS remain controversial, but are known to involve trafficking and fusion of post-Golgi vesicles. Vesicles have not been observed within the CC, and it has been proposed that vesicle transport within the CC is topologically impossible (Jin et al., 2010). An alternative model proposed that rhodopsin-containing vesicles move through the CC to fuse with nascent disks in the OS (Chuang et al., 2007), but there is little direct evidence for vesicles in the CC. At the center of this controversy lies a 30 year old debate regarding the evagination model for OS disk morphogenesis (Steinberg et al., 1980). Distinguishing among the possible mechanisms for transport and disk biosynthesis is a critical step for understanding ciliary physiology and human disease.

Retinal ciliopathies are genetic disorders causing abnormalities of photoreceptor cilia and their associated structures (Adams et al., 2007; Novarino et al., 2011), with phenotypes ranging from retinal degeneration to pleiotropic disorders such as Bardet-Biedl syndrome (BBS). Deficiencies in several proteins can result in BBS, which is a heterogeneous disorder associated with obesity, polydactyly, retinitis pigmentosa, and learning disabilities (Zaghloul and Katsanis, 2009). Mutations in BBS protein 4 (BBS4), a putative ciliary trafficking protein, result in mislocalization of OS proteins and leads to death of both rods and cones (Abd-El-Barr et al., 2007; Eichers et al., 2006; Swiderski et al., 2007). Additionally, rod OS function depends upon cGMP-gated channels located in the plasma membrane that hyperpolarize the OS in response to light. The rod-specific isoform of the β1 channel subunit, CNGB1a, encodes a unique domain, called glutamic acid rich protein (GARP), at its N-terminus which is also alternatively expressed as two soluble isoforms, GARP1 and GARP2 (Ardell et al., 2000; Korschen et al., 1995). Retinal degeneration results from mutations in BBS4, as well as CNGB1, but little distinguishes their structural phenotypes in stained electron micrographs. Such ciliopathies have unique molecular characteristics, thus it is expected that structural perturbations in rod cilia hold critical clues to disease etiology. However, the native structures and compositions of both wildtype and mutant cilia are not adequately known.

Much of our knowledge of cilia is derived from conventional electron microscopy and defined by structures exposed to fixation, staining, dehydration, and embedding, which alter cellular membranes and structures (Kellenberger et al., 1992). All structural information is then superimposed into a single projection image along the z-axis. Cryo-electron tomography (cryo-ET) allows three-dimensional (3D) reconstruction of un-fixed samples captured in their native aqueous environment (Yahav et al., 2011).

Here we present 3D structures of the wildtype rod CC, basal bodies, ciliary rootlet, and the OS, which reveal new structural features not readily observable or well preserved in

conventional electron microscopy. We investigated the structural defects in mice lacking either rootletin, a major component of the ciliary rootlet; CNGB1 and both soluble GARPs; or BBS4. Tomograms from mice with these inherited retinal neurodegenerations reveal the structural consequences, whether direct or indirect, of specific molecular deficiencies.

Results

Rod Outer Segment/Inner Segment Preparation

Figure 1A shows a schematic diagram of the structure of the rod cell, with features drawn to scale. Highlighted within the circled area is the region of the cell that is dislodged by vortexing and isolated by iso-osmotic density gradient centrifugation. Immunostaining of the cell fragments, visualized by fluorescence (Figure 1B) reveals that the OS, which stain brightly for rhodopsin, are largely intact; whereas the IS, which stain brightly for the protein rootletin, the major component of the ciliary rootlet, are broken off between the ellipsoid region of the cell (the region of the IS immediately adjacent to the OS) and the nucleus. The IS remains attached to the OS through the CC (also known as the transition zone), which does not stain with either antibody. It is well established that rhodopsin is synthesized in the IS and transported to the OS through the CC (see further evidence below), but rhodopsin does not accumulate in those regions to sufficient levels to be detected here by immunofluorescence. From such preparations, we collected a total of 145 tomograms; 76 of these were from wildtype mice.

Figure 1C shows a projection of a ~6 nm thick tomogram slice showing a portion of a rod cell containing the connecting cilium (CC), basal bodies (BB), and the ciliary rootlet (R); a segmented version of this tomogram, with continuous isodense surfaces colored for visualization, is shown in Figure 1D and Movie S1.

Adaptive Changes in Rootlet-Associated Complexes are Light-Dependent

The ciliary rootlet is the largest structure in the IS, and has previously been shown to consist primarily of the filamentous coiled-coil protein, rootletin (Yang et al., 2002). In some tomograms, such as the one shown in Figure 1F–G, pairs of 20 nm wide striations are clearly visible at inter-pair spacings of 40 nm. The position, striations, and dimensions of the rootlet correspond well to those established by conventional EM using heavy-metal stains, shown in Figure 1E. Two features of the rootlet are shown in Figure 1F–I. One is occasional branching of the rootlet, in which the branches are connected by thin fibers roughly perpendicular to the long axis of the rootlet (Figure 1F–G). The other is a set of particles, prolate ellipsoid in shape, decorating the surface of the rootlet (Figure 1G–I). These particles can be readily distinguished from phospholipid vesicles (an example of one attached to a microtubule is shown in Figure 1J–K) by their flattened shape, and by their low contrast edges (Figure 1L), which differ from the sharp density peaks due to phospholipid headgroups seen at the edges of vesicles (Figure 1M). Hypothesizing that these particles may be related to some sort of trafficking or transport process, we compared the size distributions of particles observed in cells isolated in dark-adapted and light-adapted conditions, which are known to differ greatly in rates and directions of trafficking. In the dark, the particles had a bimodal distribution with a major peak at 55 nm diameter, and a minor peak at 35 nm (Figure 1N), whereas in the light there was a single peak at about 40 nm (Figure 1O). These results suggest that the particles and their association with the rootlet are involved in the dynamic adaptive responses of rods to changes in illumination.

Pericentriolar Structures Coordinate Organelles and Transport Vesicles

When the more distal regions of the IS are examined they reveal additional features (Figure 1C–D); including endoplasmic reticulum, known from previous studies to be enriched in the

myoid region between the nucleus and the ellipsoid; and the mitochondria, previously known to be highly enriched in the ellipsoid; as well as ribosomes, identified by their shape, size, and high electron density (due to high RNA content). Some of the ribosomes are associated with rough endoplasmic reticulum. The most easily recognized organelles in this region of the IS are the basal bodies (Figure 1C–D, 2, and S1C–E), which are bounded by short (300 nm long) rings of nine microtubule triplets. The distal basal body, from which the doublets of the CC axoneme emerge, sits at the base of the CC. The proximal basal body is found nearby and is oriented roughly perpendicular to the distal basal body, but a fairly wide range of angles exists between the axes of the two basal bodies. The basal bodies are arranged with their equivalent ends close together, as seen by the opposite sense of rotation of the triplets when viewed along axes most closely aligned with the long axis of the cell (arrows in Figure 2A).

There are numerous filaments in this region of the cell, some connecting the rootlet to the basal bodies and other organelles (Figure 1C), and some connecting the basal bodies to the plasma membranes (Figure 2D). These latter filaments may correspond to a network of transition fibers identified in conventional micrographs (Deane et al., 2001). There are also numerous filaments connecting the proximal and distal basal bodies (Figure 2B–C). A filament runs up the center of the distal (axonemal) basal body (Figure 2H) and runs parallel to the microtubules. This filament is ~7 nm in diameter and 80 nm in length; and it shows a striking 8 nm periodicity, consistent with the spacing of tubulin dimers in the microtubules (Figure 2I–J and S2), though the filament does not have the correct dimensions expected for microtubules.

Many vesicle and non-vesicle cargoes converge on the CC and the pericentriolar material before they reach the OS. Every tomogram with good contrast in this distal region of the IS contains multiple vesicles. The small size of these vesicles, ranging from 30 to 100 nm in diameter, makes it difficult to capture them in conventional ultrathin sections. Invariably these vesicles are connected to filaments that extend to the plasma membrane, to the basal bodies, to the rootlet, or up into the CC (Figure 2D–F and Movie S2). Because of the high volume of membrane material trafficking from post-Golgi vesicles to the OS through the CC, it seems reasonable to propose that these vesicles are in the process of fusing with the plasma membrane of the distal IS, en route to the CC for transport via IFT or other mechanisms.

Structures of the Connecting Cilium are Compartmentalized

At the base of the CC, the triplet microtubules of the basal body (Figures 1, 2, and S2) transition to doublets, which continue as a 9 + 0 axonemal bundle through the entire transition zone and into the OS (Figure 3). Distal appendages and transition fibers extend from the C microtubules to the plasma membrane (Figure 2D–G, S2, and Movie S2). The lumen of the axoneme is not empty but contains numerous particles likely composed primarily of protein (Figure 3A–F). Although no structures resembling phospholipid vesicles were observed in the lumen of the axoneme, several tomograms contained objects whose density profiles are consistent with small (~30 nm) vesicles, located in the space between the axoneme and the CC plasma membrane (Figure 3F). Tube-like structures run parallel to the length of the axoneme between the microtubules and the plasma membrane, and appear to be aligned with the microtubules (Figure 3D–F). These tube-like structures seem connected to axoneme microtubules by additional filaments extending between both structures (green, Figure 2F–G). At the distal end of the CC, there are dense bundles of filaments extending into the proximal OS, and connecting to the edges of basal disks (Figure 3G–I). These filaments have dimensions consistent with filamentous actin, staining for which has previously been reported for this region of the cell by immuno-EM (Chaitin, 1989; Chaitin,

1992; Chaitin and Bok, 1986; Chaitin et al., 1984) and fluorescence labeling (Del Priore et al., 1987). There are also filaments in this region of the CC connecting the low density lumenal particles with the microtubules of the axoneme (Figure 3J-K, S3, and Movie S3).

The plasma membrane of the CC is not smooth, but is populated by protrusions likely corresponding to the previously described “ciliary necklace” (Figure 4). The CC plasma membrane also contains a fairly high density of rhodopsin (Figure 4C–D, S4, and Movie S4) as revealed by labeling with ferritin-tagged concanavalin A, a lectin that binds to the mannosyl residues on rhodopsin (Renthal et al., 1973). We analyzed the surface distribution of the ferritin particles on the CC surface and found good agreement with a Poisson distribution (Figure 4E), arguing against clusters of rhodopsin being transported in lipid rafts associated with IFT particles.

All Disk Membranes are Enveloped by Plasma Membrane

At the base of the OS are nascent disks, which are much smaller than disks found more distally in the OS (Figure 5B–C). Invariably, these are seen surrounded by intact plasma membrane, with no obvious continuity between the membranes of the basal disks and the plasma membrane (arrowhead in Figure 5B). Although many conventional electron micrographs have been published in which the lumen of basal disks appear open to the extracellular space, which we have also observed in a number of our collected micrographs, we have also found a number of micrographs of stained sections which are consistent with the plasma membrane enveloping the basal disks (arrowhead in Figure 5C and S5A) and a number have been previously published (e.g., (Chuang et al., 2007; Sigelman and Ozanics, 1982)). Because some of the volume of each tomogram is blurry, due to the “missing wedge” problem inherent to electron tomography, we cannot rule out that there might be small regions of continuity between disk and plasma membranes that we cannot detect. In the ferritin-concanavalin A-labeled rods with intact membranes we did not observe ferritin labeling of the disk lumen, indicating that any opening to the extracellular space is not readily traversed by objects the size of these complexes. Although they cannot rule it out unequivocally, these results challenge the widely accepted model of disk biogenesis, in which disks are thought to form by evagination of the plasma membrane, leaving the interior of the basal disks open to the extracellular space.

The disks appear much more regular in their spacings in the tomograms than in conventional electron micrographs (Figure 5). The Fourier transform of a section of stacked disks contains a series of sharp spots, corresponding to repeating units of the disk stack (Figures 5D–G and S5) with diskal spacings of 32 nm, also observed by direct measurement, and evenly divisible by the tubulin dimer repeat of 8 nm. Thus, microtubules, rather than interdisk spacers, are likely key to regulating this spacing. The quantitative features of the stacked disks, and their spatial relationships to the plasma membrane and axoneme are listed in Figure 6.

Knockout Models of Retinal Degeneration

To illustrate the ability of cryo-ET to elucidate structural defects arising from disease states, we chose three mouse models; one, *Crocc*$^{tm1Tili/tm1Tili}$, a knockout of the gene encoding rootletin, with a major defect in IS structure; one, the *Bbs4* knockout, *Bbs4*$^{Gt1Nk/Gt1Nk}$, with a major defect in the BBSome, a complex implicated in trafficking to or through the CC (Jin and Nachury, 2009; Jin et al., 2010); and one, the *Cngb1* knockout, *Cngb1*$^{tm1Sjpi/tm1Sjpi}$ with a major defect in OS structure. Each model reveals a distinct set of structural defects resulting from the distinct functions of the missing proteins.

The Rootlet Stabilizes the Cilium Axoneme

The knockout of *Crocc*, encoding rootletin, is completely missing the rootlet, which is the largest and most obvious structure in the IS (Figure 7). It has been suggested that the rootlet may play a role in positioning cellular organelles and in structural stability of the CC (Yang et al., 2005). Some tomograms of wildtype rod IS regions contain mitochondria anchored to rootlets (Figure 1C, magenta, S1C–D and hidden side of same cell in Movie S1), consistent with a role in organelle anchoring; these anchorages are obviously missing in the knockout. It has been demonstrated that the rootlet is important for photoreceptor stability, as ablation of rootletin results in progressive photoreceptor loss (Yang et al., 2005). Compared to wildtype rods, *Crocc* knockout CC are fragile and yield a five-fold increase in broken axonemes (Figure 7A–D), implying that the rootlet is important for physical stability of the CC diameter. Axial ratios (a Y:X width comparison) taken from axoneme microtubules indicate that cilia without rootletin lack structural integrity and are more compressed in reconstructed tomograms (Figure 7E–F) than are wildtype cilia; these data were collected from multiple grids for each genotype from mice of different ages (3 weeks or 18 months), ruling out sample preparation or animal age as the source of the difference.

Even in the absence of rootletin, basal bodies are correctly positioned and tethered by numerous 5 nm interconnecting fibers (Kobayashi and Dynlacht, 2011) (Figure 7C). In a small number of rootletin-lacking rods, electron-dense but poorly ordered crystalloid granules were observed in the IS surrounding the basal bodies (Figure S6). Although the molecular identity and significance of these granules is unknown, they may indicate a stress response in these rods that is absent in wildtype photoreceptors.

Loss of BBS4 Results in Altered Vesicle Distribution

Bardet-Biedl syndrome (BBS) is a pleiotropic ciliopathy associated with retinitis pigmentosa, which leads to degeneration of both rods and cones (Adams et al., 2007). An octameric complex of BBS-related proteins, called the BBSome, has been implicated in trafficking of membrane proteins in primary cilia by forming a membrane coat necessary for protein sorting (Jin et al., 2010). Tomograms from isolated *Bbs4*$^{-/-}$ rods reveal disks parallel (Figure 7G) rather than perpendicular (Figure 5A–B) to the axoneme, a hallmark of abnormal OS morphogenesis (Swiderski et al., 2007). Aberrant OS morphology may result from defective transport of protein and membrane through the CC. Supporting this hypothesis, numerous 35 nm vesicles accumulate along the axoneme, basal bodies, and IS membrane surface of *Bbs4*$^{-/-}$ rods (Figure 7H–I). These may be post-Golgi vesicles destined for the OS, which have either failed to fuse with the plasma membrane or have failed to be transported through the CC because of BBSome defects. Vesicles are absent in most tomograms of wildtype CC (see Figure 3F), possibly due to rapid transport or fusion that prevents their accumulation in the CC. In *Bbs4*$^{-/-}$ rods, fusion or transport from the base of the CC to the OS may become rate-limiting, leading to vesicle accumulation and the observed mislocalization of both cone pigments and rhodopsin (Abd-El-Barr et al., 2007).

Loss of CNGB1a and GARPs Results in Uncontrolled Disk Growth but not Altered Interdiskal Spacing

Light induces hyperpolarization of the OS by closing cGMP-gated cation channels in the OS plasma membrane. The rod-specific isoform of the β1 channel subunit, CNGB1a, encodes a unique domain, called glutamic acid rich protein (GARP), at its N-terminus which is also alternatively expressed as two soluble isoforms, GARP1 and GARP2 (Ardell et al., 2000; Korschen et al., 1995). Wildtype rod OS contain hundreds of disks evenly spaced (32 disks μm^{-1}-, Figure 6B) along the entire length of the OS (Figure 5A). Tetraspanin proteins peripherin-2 and rom-1, present at disk rims, may form an inter-membrane complex with the

CNGB1 channel in the plasma membrane. This interaction is thought to involve N-terminal GARP and possibly soluble GARP2 (Poetsch et al., 2001).

Recent identification of large spacers in tomograms of OS led to speculation that the precise interdiskal spacing is regulated by soluble GARPs (Nickell et al., 2007). Cryo-ET was carried out on rod photoreceptors lacking CNGB1 and its GARP domain, as well as both soluble GARPs (Zhang et al., 2009), and compared to tomograms of wildtype OS. Computed diffraction patterns of images of wildtype OS, exceeding 5 nm resolution from tomograms reconstructed at 1.7 nm/pixel, show precise periodic spacing of the disks (Figure 5F–G, 6B, and Figure S5). In contrast to well-organized wildtype OS that maintain their morphology during isolation (Figure 5A), *Cngb1*$^{-/-}$ rods are severely disrupted during sample preparation (Figure 7J–K). Abnormal disk size is one feature of *Cngb1*$^{-/-}$ rods (Zhang et al., 2009). Consistent with this previous observation, we find disrupted OS with diameters of ~5–6 μm in mutant rods. In these mutants, the disk membranes maintain a connection with the axoneme (Figure 7J–K) that appears normal. This observation suggests that abnormal OS diameter results from loss of disk rim connection to the plasma membrane via the channel and/or GARP. Consistent with this hypothesis, disk membranes are observed to protrude from the OS, curve, and invert back into the OS of *Cngb1*$^{-/-}$ rods (Figure 7L). Diffraction patterns of mutant disks indicate that disk spacing is not altered in the rods of either dark-adapted or light-adapted retinas (Figure 7M). These findings suggest that contact between disk rims and the plasma membrane, mediated by the CNG channel complex, is necessary to maintain accurate disk diameters, but that soluble GARP subunits do not play a significant structural role in maintaining disk spacing or attachment of disks to the axoneme.

Discussion

Previous studies of the 9 + 2 motile flagella from *Chlamydomonas reinhardtii*, have shown that cryo-ET is a powerful tool for investigating the characteristic geometry of the eukaryotic axoneme (Nicastro et al., 2006). Our 3D reconstructions of primary cilia in ice reveal a number of surprising features regarding the roles of individual disease genes, as well as insights into previously-known features. The quantitative parameters of the recurring features of the CC, which have not previously been measured accurately due to distortions from sample processing, are presented in Figure 6. Some of the characteristics of rod cilia are general for primary cilia, and some, like the stacks of disks, are specific for photoreceptors.

Rootlet structures have been identified with a number of different eukaryotic cilia including reproductive tissue (Anderson, 1972), airway epithelia (Yang et al., 2005), and hair cell stereocilia (Kitajiri et al., 2010). While rootlets are found in many ciliated cells, it is not clear whether rootletin is present in every case, nor whether the rootlet is always striated. Transport along the rootlet has not been previously reported, but we identify light-regulated changes in the dynamics of non-vesicle cargoes along the rootlet. Fibers connect the rootlet to the basal bodies, but absence of the rootlet does not alter the position of basal bodies or gross structure of the axoneme. The fragility observed at axonemal sites remote from the rootlet in rootletin-deficient rods suggests an indirect role in supplying components needed for stability. In this regard, the light-dependent dynamism of the rootlet-associated particles suggests a possible role in transport of such components. The fact that rootletin is widely expressed in mammalian tissues (Figure S1) suggests rootletin may be important for the function of many non-photoreceptor cilia as well.

Our analysis has provided a glimpse into the organization of the periciliary region surrounding the CC and reveals the complexity of these structures. In the distal IS adjacent to the CC there is a dense network of transition fibers, rootlet fibers, and distal appendages

associated with the basal bodies, transport vesicles, and periciliary plasma membrane. Transition fibers nucleate directly from basal body C-microtubules, are oriented perpendicular to the axoneme, and anchor the axoneme to the plasma membrane. We observed additional filaments, originating from either the rootlet or the IS cytoplasm, that form a filamentous/tubular structure parallel to the axoneme (Figures 2 and 3). These structures associate with vesicles and may participate in cargo sorting and transport through the CC. Many IFT-associated proteins are localized to this region (Sedmak and Wolfrum, 2010), and it is likely that the filaments play some role in assembly of cargo-bearing IFT particles, and in vesicle fusion with the plasma membrane. Defects in proteins located at the ciliary membrane, including IFT proteins, are associated with a number of retinal ciliopathies. Mutations found in members of a complex network of structural and signaling proteins result in the combined deaf-blindness phenotype of Usher's syndrome (Maerker et al., 2008). This signaling network is located at the periciliary membrane complex (Yang et al., 2010), a structure in the apical IS adjacent to the CC, which corresponds to the periciliary region in our tomograms. This complex is likely important for docking of rhodopsin transport vesicles for rhodopsin transport through the CC.

The observation of vesicles within the CC and filament-associated particles within the lumen of the axoneme suggests that transport modalities other than IFT are important for OS replenishment. Previous cryo-ET structures of flagella from *Chlamydomonas* revealed axoneme microtubules spaced ~20 nm from the flagellar membrane (Nicastro et al., 2005; Nicastro et al., 2006). While this limited space may hinder vesicle movement within the motile flagella, the analogous region is expanded to ~50 nm in the CC, which provides the potential for higher vesicle trafficking though the primary cilium. At the base of the OS, a network of actin filaments extending into the distal CC is likely involved in the sorting of molecules between plasma membrane and disks. Defects in these structures and their associated functions may be mechanisms by which ciliary defects lead to human disease. Some of these defects may be specific for photoreceptors, but it is likely that many apply to primary cilia in general and to extra-retinal symptoms of ciliopathies such as Bardet-Biedl syndrome.

The BBSome complex, which forms a membrane coat, was hypothesized to play some role in vesicle budding at the ciliary membrane (Jin et al., 2010). Our data reveal that a genetic defect in the BBSome, the BBS4 knockout, leads to a massive accumulation of vesicles rather than a dearth of them. Rather than a role in vesicle budding, the accumulation of vesicles and defective disk morphogenesis in *Bbs4*$^{-/-}$ rods suggest that a BBSsome component is required either for vesicle fusion with the plasma membrane or for vesicular transport into the CC.

The standard model for disk morphogenesis relies on an assumed continuity of the OS and CC plasma membrane with the first few basal disks, which are proposed to be formed by evagination of the plasma membrane. This standard model has previously been challenged (Chuang et al., 2007), but the recent model has proven extremely controversial. Our work sheds considerable light on this question by clearly revealing nascent basal disks, distinct from, and enclosed by the plasma membrane. Our work argues against the evagination model, but questions the alternative model (Chuang et al., 2007) in which vesicle trafficking through the CC and fusion with basal disks plays a major role in transport of rhodopsin. Hence, if rhodopsin and other disk membrane proteins are primarily transported through the plasma membrane of the CC, there must be mechanisms for moving them from the plasma membrane to nascent disks, possibly involving the actin network we describe in the distal CC.

Our work clearly rules out the proposed role of the GARP domain or free GARP as an important mediator of disk spacing or disk-microtubule interactions, as we show this interaction is normal in the absence of GARP, despite grossly misformed disk membranes in *Cngb1*$^{-/-}$ rods. Quantitative analysis of wildtype OS, by both Fourier analysis and direct measurements (Figures 5, 6, 7L-M, and S5), reveal diskal spacings of 32 nm, evenly divisible by the tubulin dimer repeat of 8 nm. Thus, microtubules, rather than interdisk spacers, are likely key to regulating this spacing. Our tomograms provide clear evidence for CNGB1 and GARPs acting as key regulators of disk size by mediating a physical connection between disk rims and the OS plasma membrane as suggested previously (Batra-Safferling et al., 2006). Loss of this critical inter-membrane connectivity is likely an important factor in the progression of retinal degeneration in *Cngb1*$^{-/-}$ mice.

Our results demonstrate the utility for using cryo-ET to characterize and compare structures of rod CC from wildtype and mutant retinas, but much more remains to be done. In the future, it seems likely that application of averaging techniques to repeating structures (Koyfman et al., 2011), with finer sampling, could improve the resolution and level of detail for structures such as the axoneme. Moreover, there are many more mouse ciliopathy models from which rods can be obtained and studied using cryo-ET. Because primary cilia are found in nearly every cell in the body, the structural insights gained from cryo-ET of photoreceptor CC have widespread implications for normal ciliary function and for the etiology of pleiotropic ciliopathies. The identification by cryo-ET of structural perturbations resulting from additional specific gene defects, can help to elucidate the structural and functional roles of the corresponding gene products, and contribute to development of a complete molecular description of primary cilium structure and function.

Experimental Procedures

Animals

All animals were handled according to NIH guidelines and all procedures used were approved by the Institutional Animal Care and Use Committees of the institutions involved. Wildtype C57Bl/6 and ciliopathy mutant mice were used in this study; *Crocc*$^{-/-}$ (Yang et al., 2005), *Bbs4*$^{-/-}$ (Eichers et al., 2006), and *Cngb1*$^{-/-}$ (Zhang et al., 2009) were described previously.

Molecular identification

Procedures and reagents for tissue preparation, immunostaining, and Northern blotting are described in Supplementary Content.

Isolation of Rod Outer Segments

All procedures were performed in the dark using infrared illumination and detection for dark-adapted mice or under room light for light-adapted mice. Dark-adapted mice were maintained in constant darkness for 12 hr overnight prior to rod OS isolation. Retinas from 6–12 mice were isolated from 21 day old or 18 month old (WT), 33 day old (*Bbs4*$^{-/-}$ and *Cngb1*$^{-/-}$), or 18 month old (*Crocc*$^{-/-}$) genotypes in 250 μL iso-osmotic Ringer's buffer (10 mM HEPES, 130 mM NaCl, 3.6 mM KCl, 12 mM $MgCl_2$, 1.2 mM $CaCl_2$, 0.02 mM EDTA, pH 7.4) with 8% (vol/vol) OptiPrep (Axis-Shield). Retinas were vortexed at low speed for 1 min, centrifuged at 200 × g for 1 min, and supernatants were collected on ice. The process was repeated 5 times before layering OS on a 10–30% (vol/vol) discontinuous OptiPrep gradient and centrifuged 60 min at 24,700 × g at 4°C using a TLS 55 rotor in an Optima Ultracentrifu ge (Beckman Coulter). Intact OS band was collected, diluted in Ringer's buffer, and pelleted in a TLA 100.3 rotor for 30 min at 26,500 × g at 4°C. OS were resuspended in Ringer's buffer. Inta ct OS were applied to 200 mesh holey carbon grids

(Quantifoil, Germany) and incubated for 10 s before blotting with filter paper and vitrification in liquid ethane at −196°C using the Vitrobot Mark III (FEI, Hillsboro, OR).

Cryo-ET and Image Processing

OS grids were imaged at −180°C with SerialEM softwa re (Mastronarde, 2005) in a JEM2100 electron microscope (JEOL, Tokyo, Japan) operated between 20,000× and 30,000× magnification at 200 KV. Single-axis tilt series were collected between ±60° at 2° increments with a cumulative dose of 50–100 $e^{-}/Å^2$ at 7–12 μm defocus. Data were acquired using a 4096 × 4096 pixel charge-coupled device camera (Gatan, Pleasanton, CA). Micrograph alignment and 3D tomographic reconstruction were performed with IMOD software using gold markers (Mastronarde, 1997). Manual volume segmentation was performed using the Amira software package (Visage Imaging, San Diego, CA). Tomogram measurements and Fourier analysis were carried out using a combination of IMOD and ImageJ (Abramoff et al., 2004).

Electron Microscopy of Ultra-Thin Sections

Eyecups were treated with fixative, rinsed in Cacodylate buffer, and post-fixed with osmium tetroxide. Eyecups were rinsed several times and dehydrated in a graded ethanol series prior to epon resin embedding. Ultrathin sections (80 nm thick) were cut and mounted on 100 mesh copper grids and stained with 2% uranyl acetate and Reynold's lead citrate. Electron micrographs were captured in a Zeiss CEM 902 electron microscope on Kodak (Rochester, NY) 4489 EM film. Extensive method is described in Supplementary material.

Accession Numbers

Eight representative tomograms have been deposited with the EMDataBank (http://www.emdatabank.org/) with accession numbers for wildtype (EMD-5477, EMD-5478, EMD-5479, EMD-5480, EMD-5481) and knockout (EMD-5482, EMD-5483, EMD-5484) data. The remaining tomograms and individual image files will be made available upon request.

Supplementary Material

Refer to Web version on PubMed Central for supplementary material.

Acknowledgments

This work was supported in part by grants from the NIH (EY011900 and EY07981 to TGW, P41RR002250 to WC, EY018143 to SJP, EY10309, EY10581 to TL, support for IMS by EY011731, an NIH NRSA trainee appointment on grant T32EY007001 to JCG, and Vision Research Core Grant EY002520), and by the Robert Welch Foundation (Q-0035 to TGW, Q1242 to WC). We thank Mr. Ralph Nichols for help with electron microscopy of fixed samples, and Dr. Vera Moiseenkova-Bell for help in the early stages of the project, and Dr. Alecia Gross for helpful suggestions and pilot experiments.

References

Abd-El-Barr MM, Sykoudis K, Andrabi S, Eichers ER, Pennesi ME, Tan PL, Wilson JH, Katsanis N, Lupski JR, Wu SM. Impaired photoreceptor protein transport and synaptic transmission in a mouse model of Bardet-Biedl syndrome. Vision Res. 2007; 47:3394–3407. [PubMed: 18022666]

Abramoff MD, Magelhaes PJ, Ram SJ. Image Processing with ImageJ. Biophotonics International. 2004; 11:36–42.

Adams NA, Awadein A, Toma HS. The retinal ciliopathies. Ophthalmic Genet. 2007; 28:113–125. [PubMed: 17896309]

Anderson RG. The three-dimensional structure of the basal body from the rhesus monkey oviduct. J Cell Biol. 1972; 54:246–265. [PubMed: 5064817]

Ardell MD, Bedsole DL, Schoborg RV, Pittler SJ. Genomic organization of the human rod photoreceptor cGMP-gated cation channel beta-subunit gene. Gene. 2000; 245:311–318. [PubMed: 10717482]

Batra-Safferling R, Abarca-Heidemann K, Korschen HG, Tziatzios C, Stoldt M, Budyak I, Willbold D, Schwalbe H, Klein-Seetharaman J, Kaupp UB. Glutamic acid-rich proteins of rod photoreceptors are natively unfolded. J Biol Chem. 2006; 281:1449–1460. [PubMed: 16280326]

Calvert PD, Schiesser WE, Pugh EN Jr. Diffusion of a soluble protein, photoactivatable GFP, through a sensory cilium. J Gen Physiol. 2010; 135:173–196. [PubMed: 20176852]

Chaitin MH. Immunogold localization of actin and opsin in rds mouse photoreceptors. Prog Clin Biol Res. 1989; 314:265–274. [PubMed: 2532745]

Chaitin MH. Double immunogold localization of opsin and actin in the cilium of developing mouse photoreceptors. Exp Eye Res. 1992; 54:261–267. [PubMed: 1532781]

Chaitin MH, Bok D. Immunoferritin localization of actin in retinal photoreceptors. Invest Ophthalmol Vis Sci. 1986; 27:1764–1767. [PubMed: 3793408]

Chaitin MH, Schneider BG, Hall MO, Papermaster DS. Actin in the photoreceptor connecting cilium: immunocytochemical localization to the site of outer segment disk formation. J Cell Biol. 1984; 99:239–247. [PubMed: 6610682]

Chuang JZ, Zhao Y, Sung CH. SARA-regulated vesicular targeting underlies formation of the light-sensing organelle in mammalian rods. Cell. 2007; 130:535–547. [PubMed: 17693260]

Clarke RD. An application of the Poisson distribution. Journal of the Institute of Actuaries. 1946; 72:481.

Deane JA, Cole DG, Seeley ES, Diener DR, Rosenbaum JL. Localization of intraflagellar transport protein IFT52 identifies basal body transitional fibers as the docking site for IFT particles. Curr Biol. 2001; 11:1586–1590. [PubMed: 11676918]

Del Priore LV, Lewis A, Tan S, Carley WW, Webb WW. Fluorescence light microscopy of F-actin in retinal rods and glial cells. Invest Ophthalmol Vis Sci. 1987; 28:633–639. [PubMed: 3104228]

Eichers ER, Abd-El-Barr MM, Paylor R, Lewis RA, Bi W, Lin X, Meehan TP, Stockton DW, Wu SM, Lindsay E, et al. Phenotypic characterization of Bbs4 null mice reveals age-dependent penetrance and variable expressivity. Hum Genet. 2006; 120:211–226. [PubMed: 16794820]

Gherman A, Davis EE, Katsanis N. The ciliary proteome database: an integrated community resource for the genetic and functional dissection of cilia. Nat Genet. 2006; 38:961–962. [PubMed: 16940995]

Jin H, Nachury MV. The BBSome. Curr Biol. 2009; 19:R472–473. [PubMed: 19549489]

Jin H, White SR, Shida T, Schulz S, Aguiar M, Gygi SP, Bazan JF, Nachury MV. The conserved Bardet-Biedl syndrome proteins assemble a coat that traffics membrane proteins to cilia. Cell. 2010; 141:1208–1219. [PubMed: 20603001]

Kellenberger E, Johansen R, Maeder M, Bohrmann B, Stauffer E, Villiger W. Artefacts and morphological changes during chemical fixation. J Microsc. 1992; 168:181–201. [PubMed: 1464902]

Kim JC, Badano JL, Sibold S, Esmail MA, Hill J, Hoskins BE, Leitch CC, Venner K, Ansley SJ, Ross AJ, et al. The Bardet-Biedl protein BBS4 targets cargo to the pericentriolar region and is required for microtubule anchoring and cell cycle progression. Nat Genet. 2004; 36:462–470. [PubMed: 15107855]

Kitajiri S, Sakamoto T, Belyantseva IA, Goodyear RJ, Stepanyan R, Fujiwara I, Bird JE, Riazuddin S, Riazuddin S, Ahmed ZM, et al. Actin-bundling protein TRIOBP forms resilient rootlets of hair cell stereocilia essential for hearing. Cell. 2010; 141:786–798. [PubMed: 20510926]

Kobayashi T, Dynlacht BD. Regulating the transition from centriole to basal body. J Cell Biol. 2011; 193:435–444. [PubMed: 21536747]

Korschen HG, Illing M, Seifert R, Sesti F, Williams A, Gotzes S, Colville C, Muller F, Dose A, Godde M, et al. A 240 kDa protein represents the complete beta subunit of the cyclic nucleotide-gated channel from rod photoreceptor. Neuron. 1995; 15:627–636. [PubMed: 7546742]

Koyfman AY, Schmid MF, Gheiratmand L, Fu CJ, Khant HA, Huang D, He CY, Chiu W. Structure of Trypanosoma brucei flagellum accounts for its bihelical motion. Proc Natl Acad Sci U S A. 2011; 108:11105–11108. [PubMed: 21690369]

Kozminski KG, Johnson KA, Forscher P, Rosenbaum JL. A motility in the eukaryotic flagellum unrelated to flagellar beating. Proc Natl Acad Sci U S A. 1993; 90:5519–5523. [PubMed: 8516294]

LaVail MM. Rod outer segment disk shedding in rat retina: relationship to cyclic lighting. Science. 1976; 194:1071–1074. [PubMed: 982063]

Liu Q, Tan G, Levenkova N, Li T, Pugh EN Jr, Rux JJ, Speicher DW, Pierce EA. The proteome of the mouse photoreceptor sensory cilium complex. Mol Cell Proteomics. 2007; 6:1299–1317. [PubMed: 17494944]

Maerker T, van Wijk E, Overlack N, Kersten FF, McGee J, Goldmann T, Sehn E, Roepman R, Walsh EJ, Kremer H, Wolfrum U. A novel Usher protein network at the periciliary reloading point between molecular transport machineries in vertebrate photoreceptor cells. Hum Mol Genet. 2008; 17:71–86. [PubMed: 17906286]

Mastronarde DN. Dual-axis tomography: an approach with alignment methods that preserve resolution. J Struct Biol. 1997; 120:343–352. [PubMed: 9441937]

Mastronarde DN. Automated electron microscope tomography using robust prediction of specimen movements. J Struct Biol. 2005; 152:36–51. [PubMed: 16182563]

Mayer U, Kuller A, Daiber PC, Neudorf I, Warnken U, Schnolzer M, Frings S, Mohrlen F. The proteome of rat olfactory sensory cilia. Proteomics. 2009; 9:322–334. [PubMed: 19086097]

Moser JJ, Fritzler MJ, Ou Y, Rattner JB. The PCM-basal body/primary cilium coalition. Semin Cell Dev Biol. 2009; 21:148–155. [PubMed: 19591955]

Nachury MV, Seeley ES, Jin H. Trafficking to the ciliary membrane: how to get across the periciliary diffusion barrier? Annu Rev Cell Dev Biol. 2010; 26:59–87. [PubMed: 19575670]

Nair KS, Hanson SM, Mendez A, Gurevich EV, Kennedy MJ, Shestopalov VI, Vishnivetskiy SA, Chen J, Hurley JB, Gurevich VV, Slepak VZ. Light-dependent redistribution of arrestin in vertebrate rods is an energy-independent process governed by protein-protein interactions. Neuron. 2005; 46:555–567. [PubMed: 15944125]

Nicastro D, McIntosh JR, Baumeister W. 3D structure of eukaryotic flagella in a quiescent state revealed by cryo-electron tomography. Proc Natl Acad Sci U S A. 2005; 102:15889–15894. [PubMed: 16246999]

Nicastro D, Schwartz C, Pierson J, Gaudette R, Porter ME, McIntosh JR. The molecular architecture of axonemes revealed by cryoelectron tomography. Science. 2006; 313:944–948. [PubMed: 16917055]

Nickell S, Park PS, Baumeister W, Palczewski K. Three-dimensional architecture of murine rod outer segments determined by cryoelectron tomography. J Cell Biol. 2007; 177:917–925. [PubMed: 17535966]

Novarino G, Akizu N, Gleeson JG. Modeling human disease in humans: the ciliopathies. Cell. 2011; 147:70–79. [PubMed: 21962508]

Ostrowski LE, Blackburn K, Radde KM, Moyer MB, Schlatzer DM, Moseley A, Boucher RC. A proteomic analysis of human cilia: identification of novel components. Mol Cell Proteomics. 2002; 1:451–465. [PubMed: 12169685]

Pazour GJ, Baker SA, Deane JA, Cole DG, Dickert BL, Rosenbaum JL, Witman GB, Besharse JC. The intraflagellar transport protein, IFT88, is essential for vertebrate photoreceptor assembly and maintenance. J Cell Biol. 2002; 157:103–113. [PubMed: 11916979]

Poetsch A, Molday LL, Molday RS. The cGMP-gated channel and related glutamic acid-rich proteins interact with peripherin-2 at the rim region of rod photoreceptor disc membranes. J Biol Chem. 2001; 276:48009–48016. [PubMed: 11641407]

Renthal R, Steinemann A, Stryer L. The carbohydrate moiety of rhodopsin: lectin-binding, chemical modification and fluorescence studies. Exp Eye Res. 1973; 17:511–515. [PubMed: 4361169]

Sedmak T, Wolfrum U. Intraflagellar transport molecules in ciliary and nonciliary cells of the retina. J Cell Biol. 2010; 189:171–186. [PubMed: 20368623]

Sigelman, J.; Ozanics, V. Chapter 15 “Retina”. In: Jakobiec, FA., editor. Ocular Anatomy, Embryology and Teratology. Philadelphia; Harper & Row: 1982. p. 462

Spira AW, Milman GE. The structure and distribution of the cross-striated fibril and associated membranes in guinea pig photoreceptors. Am J Anat. 1979; 155:319–337. [PubMed: 573060]

Steinberg RH, Fisher SK, Anderson DH. Disc morphogenesis in vertebrate photoreceptors. J Comp Neurol. 1980; 190:501–508. [PubMed: 6771304]

Swiderski RE, Nishimura DY, Mullins RF, Olvera MA, Ross JL, Huang J, Stone EM, Sheffield VC. Gene expression analysis of photoreceptor cell loss in bbs4-knockout mice reveals an early stress gene response and photoreceptor cell damage. Invest Ophthalmol Vis Sci. 2007; 48:3329–3340. [PubMed: 17591906]

Yahav T, Maimon T, Grossman E, Dahan I, Medalia O. Cryo-electron tomography: gaining insight into cellular processes by structural approaches. Curr Opin Struct Biol. 2011

Yang J, Gao J, Adamian M, Wen XH, Pawlyk B, Zhang L, Sanderson MJ, Zuo J, Makino CL, Li T. The ciliary rootlet maintains long-term stability of sensory cilia. Mol Cell Biol. 2005; 25:4129–4137. [PubMed: 15870283]

Yang J, Li T. The ciliary rootlet interacts with kinesin light chains and may provide a scaffold for kinesin-1 vesicular cargos. Exp Cell Res. 2005; 309:379–389. [PubMed: 16018997]

Yang J, Liu X, Yue G, Adamian M, Bulgakov O, Li T. Rootletin, a novel coiled-coil protein, is a structural component of the ciliary rootlet. J Cell Biol. 2002; 159:431–440. [PubMed: 12427867]

Yang J, Liu X, Zhao Y, Adamian M, Pawlyk B, Sun X, McMillan DR, Liberman MC, Li T. Ablation of whirlin long isoform disrupts the USH2 protein complex and causes vision and hearing loss. PLoS Genet. 2010; 6:e1000955. [PubMed: 20502675]

Young RW. The renewal of photoreceptor cell outer segments. J Cell Biol. 1967; 33:61–72. [PubMed: 6033942]

Zaghloul NA, Katsanis N. Mechanistic insights into Bardet-Biedl syndrome, a model ciliopathy. J Clin Invest. 2009; 119:428–437. [PubMed: 19252258]

Zhang Y, Molday LL, Molday RS, Sarfare SS, Woodruff ML, Fain GL, Kraft TW, Pittler SJ. Knockout of GARPs and the beta-subunit of the rod cGMP-gated channel disrupts disk morphogenesis and rod outer segment structural integrity. J Cell Sci. 2009; 122:1192–1200. [PubMed: 19339551]

Highlights

- 3D structures of primary cilia from wildtype and mutant rod cells.
- Multiple transport modes in different compartments.
- Basal disks form within plasma membrane.
- Genetic defects alter trafficking and structural organization of primary cilia.

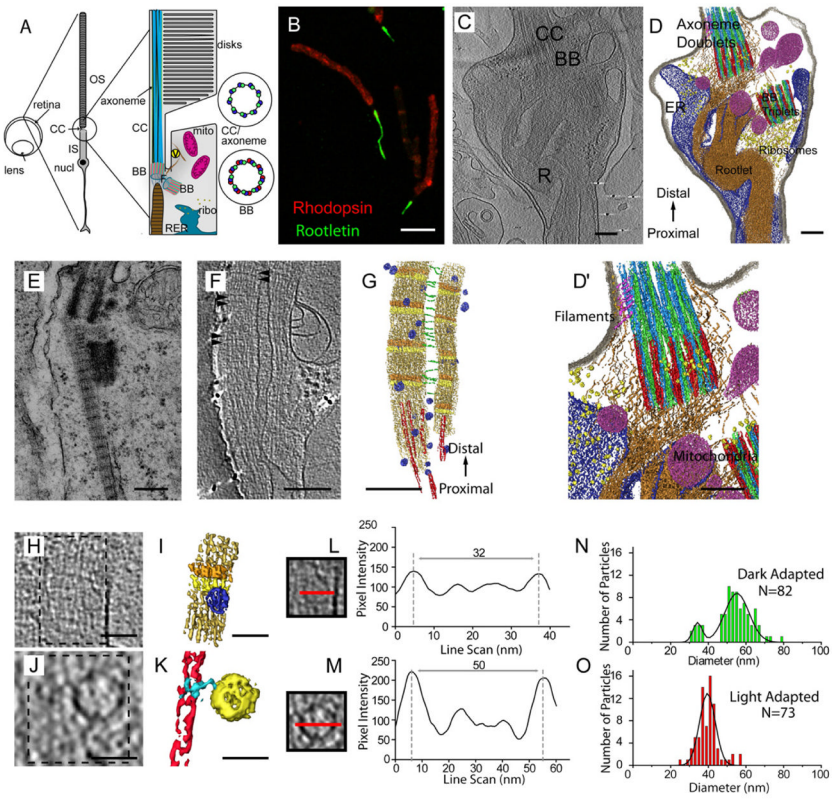

Figure 1. Cilium-Associated Structures in the Rod IS

(A) Diagram of rod cell and regions adjacent to the connecting cilium.

(B) Immunofluorescence of isolated rod OS/IS preparation stained with antibodies specific for rhodopsin (red) and rootletin (green). Bar = 5 μm

(C) Projection (6 nm thick) from a tomogram of the IS ellipsoid region and adjacent structures of the connecting cilium (CC), basal bodies (BB), and rootlet (R). Bars in (C–D) = 0.1 μm.

(D) Segmented version of tomogram shown in (C). Microtubules (light blue, A MT; green, B MT; red, C MT), axoneme filaments/transition fibers (pink), rootlet (brown), plasma membrane (gray), endoplasmic reticulum (dark blue), mitochondria (magenta), ribosomes (yellow).

(E) Conventional EM image of stained ultrathin section of mouse retina showing a typically striated ciliary rootlet terminating near the proximal basal body. Bar = 0.2 μm.

(F) Tomogram Projection of a ciliary rootlet. Bars in (F–G) = 0.1 μm.

(G) Segmented version of (F), showing rootlet, striations (arrowheads in (F), orange/yellow in (G) and (I)), filaments (green), and non-vesicle rootlet-associated particles (blue).

(H and I) Enlarged region of tomogram with rootlet-attached particle, segmented in (I). Bars = 50 nm.

(J and K) Tomogram and segmentation of microtubule with attached vesicle. Bars = 50 nm.

(L and M) Axial density profiles of particle (L) and vesicle (M) taken from (H) and (J).

(N and O) Histograms of rootlet-associated particle diameters measured in rods from (N) dark- and (O) light-adapted retinas. N = total particles per condition.

(See also Figure S1 and Movie S1)

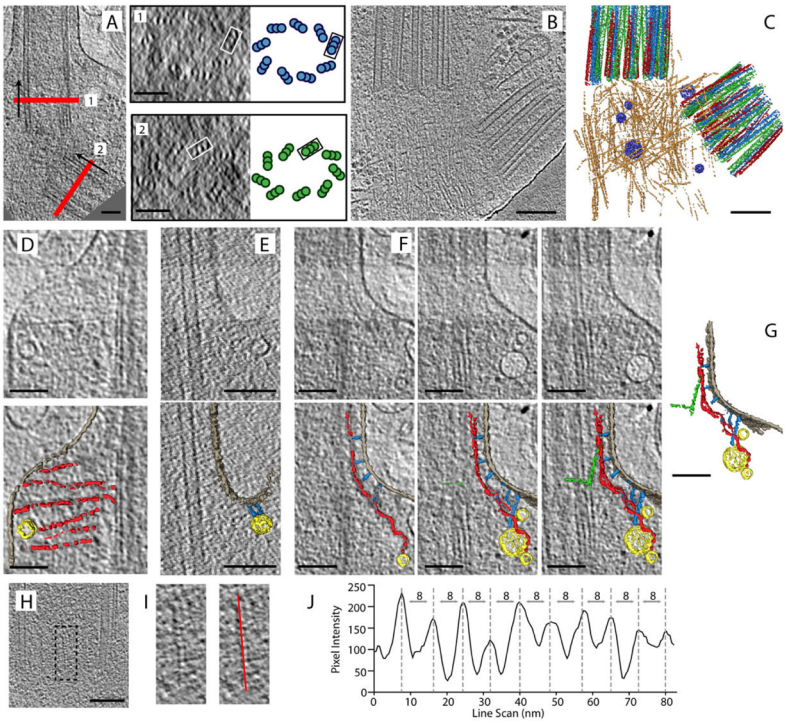

Figure 2. Structures of the Distal IS

(A) Tomogram projection of wildtype basal bodies. Cross-section slices (red lines) through the distal (A1) and proximal (A2) basal bodies along the z-axis (proximal-to-distal direction indicated by black arrows) show opposite rotation polarity of microtubule triplets, as indicated in the diagrams [right]. All bars = 0.1 μm.

(B and C) Tomogram projection and segmentation of basal bodies, rootlet fibers, and non-vesicle particles from the wildtype rod IS. Microtubules (green, blue, red), rootlet filaments (brown), and rootlet particles (blue).

(D–F) Multiple projections shown as raw data [top] or annotated [bottom] by segmentation. D and F are from the cell in (A).

(D) Transition fibers (red) originate from [outermost] C-microtubules of basal body triplets and extend horizontally to the plasma membrane where vesicles (yellow) are located.

(E) Vesicles (yellow) are tethered to the plasma membrane by filamentous proteins (blue).

(F) Panel of three consecutive tomographic slices. From C-microtubules extend distal appendages (green) that extend both radially to neighboring microtubules and distally into the cilium. Filaments originating from the IS (red) interact with vesicles (yellow), C-microtubule distal appendages (green), and ciliary membrane filaments (blue).

(G) Segmentation from (F) of vesicles (yellow), IS filaments (red), distal appendages (green), and membrane tethers (blue) in the pericentriolar region.

(H) Tomogram projection through the axoneme basal body shows 80 nm long rootlet filaments (black box) extending into axoneme center. All bars = 0.1 μm.

(I) Magnification of bounded area from (H) shows multiple filament densities.

(J) Density profile of the filament (indicated by red line in (I)).

(See also Figure S2 and Movie S2)

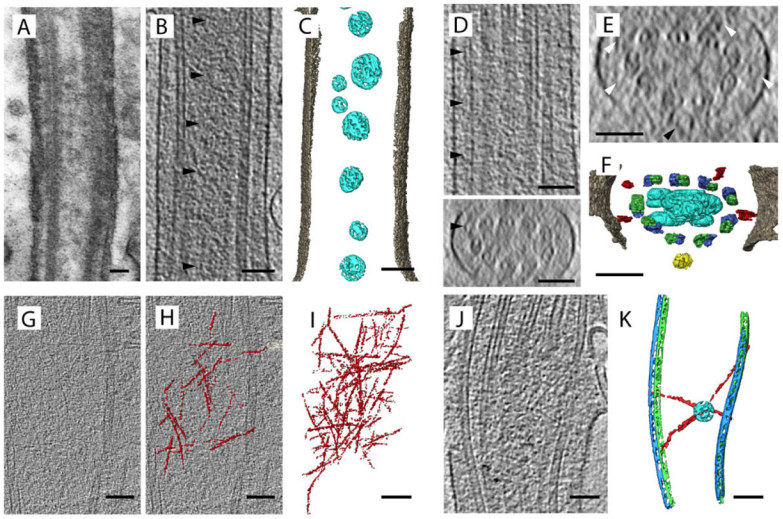

Figure 3. Structures of the Connecting Cilium

(A) Conventional EM image of the CC from stained rods. All bars = 0.1 μm.

(B and C) Tomogram and segmentation of the wildtype CC reveal low-contrast particles (arrowheads in (B)) bounded by microtubules in the central axoneme compartment. CC membrane (gray), and particles (cyan).

(D) Tomogram projections through the wildtype CC in the X–Y plane [top] and X–Z plane cross-section [bottom] resolve 20 nm tubules extending the length of the CC, parallel to the axoneme. Tubule is limited to the outer-axonemal space (arrowheads).

(E) Tomogram projection of CC cross-section showing 20 nm tubules [white arrowheads] parallel to axoneme microtubules. One vesicle is shown between the axoneme and the plasma membrane [black arrowhead].

(F) Segmentation from (E) of membrane (gray), microtubules (green, blue), particles (cyan), tubule (red), and vesicle (yellow) in the wildtype CC.

(G and H) Tomogram and segmentation overlay of filaments (red) anchoring disk rim (white) at the OS base to axoneme microtubules of the CC.

(I) Segmentation of filaments from (B).

(J and K) Tomogram and segmentation of low-contrast particle bound to actin-like filaments in the CC just below the region of nascent OS disk formation. Microtubules (green, blue), actin (red), and particle (cyan).

(See also Figure S3 and Movie S3)

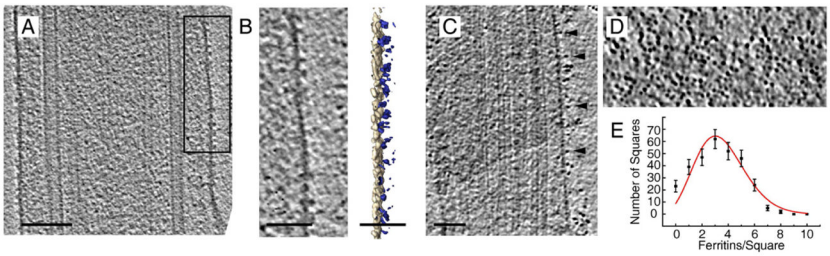

Figure 4. Structures Associated with the Ciliary Membrane

(A) Protein densities in the CC membrane. Bar = 0.1 μm.

(B) Tomogram and segmentation of membrane densities (box in (A)). Membrane (gray), and proteins (blue). Bars = 50 nm.

(C) Concanavalin A-ferritin labels rhodopsin N-termini in a tomogram projection through the CC. Stalk-like protrusions seen in (A) and (B) labeled with ferritin (arrowheads). Bar = 0.1 μm.

(D) Tomogram of the CC membrane surface with rhodopsin labeled with concanavalin A-ferritin.

(E) Histogram of rhodopsin-ferritin distribution within the ciliary membrane. A 0.27 μm^2 region of membrane was divided into 300 equal squares, and the number of ferritins in each counted (952 = total). The curve is the expectation for a random distribution (Clarke, 1946). (See also Figure S4 and Movie S4)

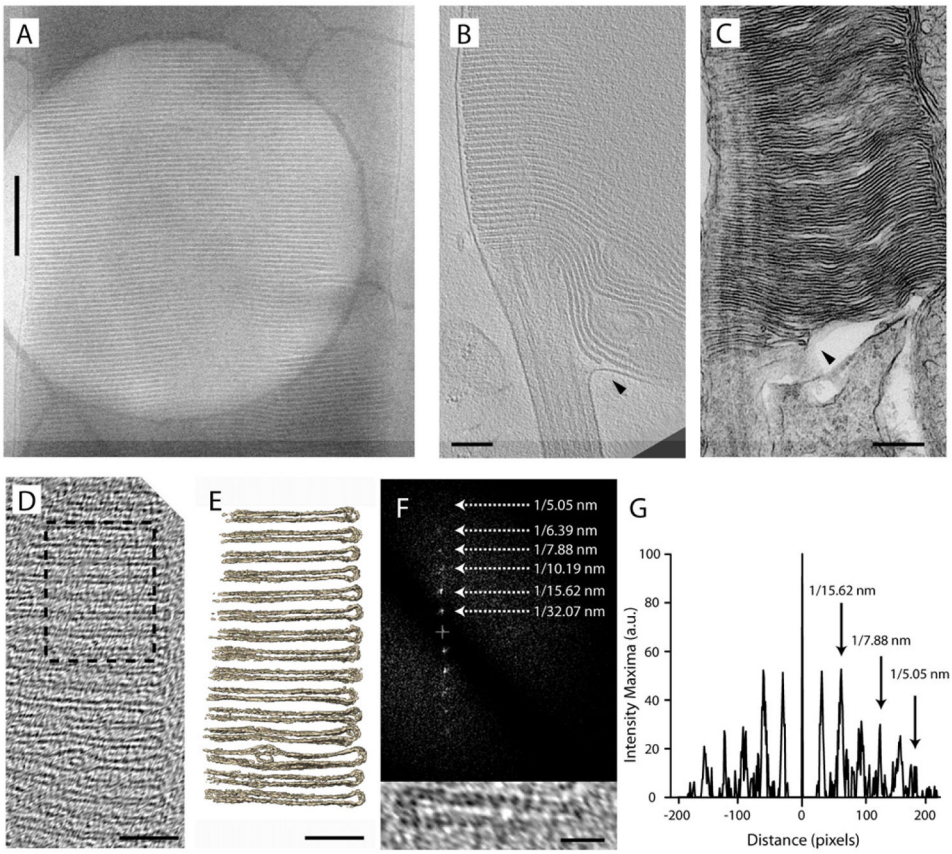

Figure 5. Structures of the Outer Segment

(A) Micrograph of a vitrified rod OS shows spacing of 32 disks per μm. Bar = 0.5 μm.

(B) Cryo-ET preserves the native structural organization of rod OS. Nascent disk contained within the OS plasma membrane (arrowhead). Bar = 0.2 μm.

(C) Conventional micrograph of a stained rod shows nascent disks contained within the OS plasma membrane (arrowhead). Bar = 0.4 μm.

(D and E) Tomogram and segmentation of wildtype OS disk stack. Bar = 0.1 μm.

(F) Fourier transform (computed diffraction pattern) from dashed box in (D) indicates up to 6 intensity maxima in reciprocal space [top]. Analysis performed on tomogram with 1.7 nm/pixel resolution. The highest resolution obtained (1/5.05 nm) corresponds to the bilayer thickness of the OS disk [bottom]. Bar = 15 nm.

(G) Frequency spectrum of maxima in (F) confirms 6 discrete peaks are present in the data. (See also Figure S5)

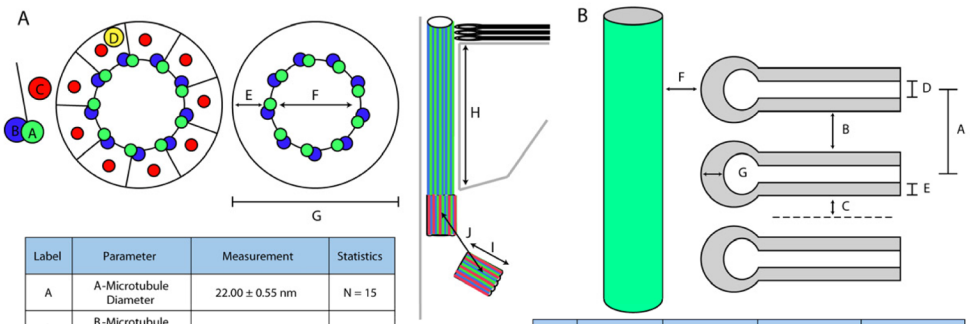

Label	Parameter	Measurement	Statistics
A	A-Microtubule Diameter	22.00 ± 0.55 nm	N = 15
B	B-Microtubule Diameter	24.17 ± 0.44 nm	N = 9
C	Tubule Diameter	20.22 ± 0.58 nm	N = 9
D	Vesicle Diameter	35.56 ± 2.04 nm	N = 16
E	MT-to-PM Distance	50.59 ± 2.19 nm	N = 10
F	Axoneme Inner-Diameter	156.26 ± 4.85 nm	N = 6
G	Connecting Cilium Diameter	302.02 ± 11.93 nm	N = 9
H	Ciliary Membrane Length	1112.1 ± 40.09 nm	N = 12
I	Basal Body Length	302.25 ± 6.89 nm	N = 11
J	BB-to-BB Distance	516.1 ± 131.0 nm	N = 20

Label	Parameter	Diffraction Pattern	Measurement	Statistics
A	Disk Interval	1/32.07 nm	32 μm^{-1}	64 consecutive disks
B	Inter-Disk Spacing	1/15.62 nm	15.56 ± 0.94 nm	N = 24
C	Inter-Disk Density	1/7.88 nm	7.81 ± 0.31 nm	N = 19
D	Intra-Disk Spacing	1/6.39 n m	6.36 ± 0.86 nm	N = 19
E	Disk Bilayer Thickness	1/5.05 nm	5.01 ± 0.52 nm	N = 40
F	Disk to Microtubule	N/A	14.69 ± 0.53 nm	N = 22
N/A	Disk to Membrane	N/A	18.18 ± 2.36 nm	N = 25
G	Disk Rim Thickness	N/A	8.21 ± 0.46 nm	N = 11

Figure 6. Quantitative Summary of Structural Features

Measurements of the CC (A) and the OS (B) features. Direct measurements are provided as mean ± standard deviation. N, = total measurements collected per parameter.

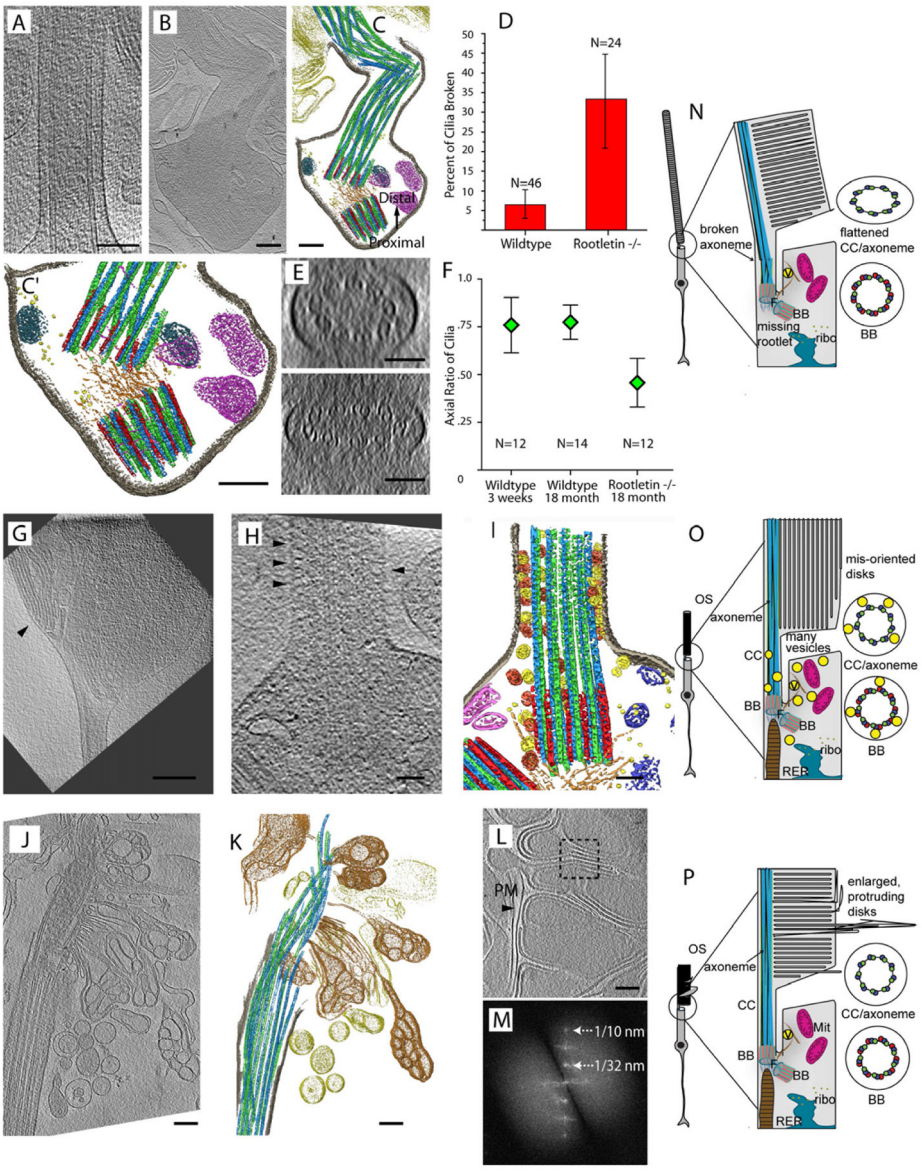

Figure 7. Structural Perturbations Caused By Genetic Defects

(A and B) Tomogram projections from wildtype (A) and *Crocc*$^{-/-}$ (B) cilia. Bars (A–C′) = 0.2 μm.

(C and C′) Structural differences in *Crocc*$^{-/-}$ cilia lead to fragile axonemes. Segmentation of basal bodies and filaments from (B). Microtubules (green, blue, red), interconnecting filaments (orange), plasma membrane (gray), organelle (likely ER and mitochondria) membranes (magenta, blue), ribosomes (yellow), and disrupted OS disks (yellow, left side and upper right corner).

(D) Histogram of broken axonemes in tomograms from wildtype and *Crocc*$^{-/-}$ cilia. N = number of tomograms for each genotype. Error bars represent Poisson statistics for N.

(E) Projection (~30 nm thick) of wildtype [top] and *Crocc*$^{-/-}$ [bottom] cilia. Bar = 0.1 μm.

(F) Altered axial ratios from *Crocc*$^{-/-}$ cilia indicate structural defects in mutant axonemes. N = number of axonemes measured for each genotype. Data are mean ± standard deviation.

(G) Tomogram of the OS from a *Bbs4*$^{-/-}$ rod shows altered disk orientation and morphology (arrowhead). Bar = 0.4 μm.

(H and I) Tomogram and segmentation of the *Bbs4*$^{-/-}$ CC reveals vesicles accumulated along the axoneme. Microtubules (green, blue, red), plasma membrane (gray), and vesicles (yellow, pink). Bar = 50 nm.
(J and K) Tomogram and segmentation of the *Cngb1*$^{-/-}$ rod indicates disrupted OS membrane structure resulting from aberrant growth of OS disks. Microtubules (green, blue), plasma membrane (gray), and OS disks (yellow, gold). Bar = 0.2 μm.
(L) Tomogram projection of the *Cngb1*$^{-/-}$ OS shows excessive disk growth is caused by lack of contact between the plasma membrane (PM) and disk rims.
(M) Fourier transform from dashed box in (L) yields three intensity maxima, indicating normal disk spacing in *Cngb1*$^{-/-}$ OS. Bar = 0.2 μm.
(N) Diagram of perturbations found in *Crocc*$^{-/-}$ rod cells.
(O) Diagram of perturbations found in *Bbs4*$^{-/-}$ rod cells
(P) Diagram of perturbations found in *Cngb1*$^{-/-}$ rod cells
(See also Figure S6)